IET Journals
The Institution of Engineering and Technology

Excitation and coupling of volume and surface fields on complex electrodynamic surfaces at mm-wave and THz frequencies

Amy J. MacLachlan[1], Craig W. Robertson[1], Adrian W. Cross[1], Kevin Ronald[1], Alan D.R. Phelps[1] ✉

[1]Department of Physics, SUPA, University of Strathclyde, Glasgow, G4 0NG, Scotland, UK
✉ E-mail: a.d.r.phelps@strath.ac.uk

Abstract: The analytical theory describing the resonant excitation and coupling of volume and surface fields on the surface of two-dimensional complex electrodynamic structures is presented. The theoretical analysis is valid over a broad frequency spectrum from mm-wave frequencies through THz and even optical frequencies. An experimental study of planar periodic structures has been carried out using a vector network analyser calibrated to operate in the 140–220 GHz frequency range. Experimental results compare resonant eigenmode formation in two periodic surface lattice structures designed to operate within the 140–220 GHz frequency band; one periodic surface lattice etched onto a metal-backed substrate and the other arranged to have an equivalent air separation. Dispersion diagrams derived from the analytical theory are presented. The results and theory are fundamental to some of the routes to the innovation of high-power, mm-wave and THz sources, solar cells, and novel sub-wavelength absorbers.

1 Introduction

Periodic structures, both one- and two-dimensional (1D and 2D), have importance in 'fast-wave' and 'slow-wave' applications, for instance in free-electron lasers where they can be implemented as Bragg reflectors. Historically, periodic structures of coaxial, cylindrical, and planar geometries have been studied [1–9]. The current work, which concerns 2D planar and cylindrical periodic surface lattice (PSL) structures, is driven by the desire for highly overmoded high-power 'slow-wave' (Cherenkov) sources of electromagnetic radiation. However, the theoretical, numerical, and experimental results are also relevant to a number of other electromagnetic applications. One of the defining and most interesting properties of the 2D PSL structures of both geometries is the observation of volume and surface fields, which co-exist at the corrugated metal boundary and under suitable conditions [2–7], can couple to produce a single cavity eigenfield. This eigenfield, composed of 'partial' volume and surface fields, is the means through which single-mode excitation in the oversized and highly overmoded cavity is achieved. An important physical characteristic of the 2D PSL structures is that the depth of the corrugation must be small in relation to the source wavelength. When this transverse dimension is less than an electromagnetic wavelength, the PSL can be likened to an effective 'meta-dielectric', which supports a unique hybrid eigenfield. High-power radiation sources at mm-wave and THz frequencies can be constructed by passing an appropriate electron beam close to the corrugated walls to facilitate a successful interaction between the electron beam and the eigenfield of the PSL. The theory also applies to frequencies beyond the mm-wave and THz regions and extends, e.g. to optical frequencies where Cherenkov radiation can be produced by the exploitation of surface polaritons [10]. The PSL structures are suited to applications in solar cells [11], novel sub-wavelength absorbers [12, 13], compact antennae [14], and electromagnetic filters [15–18] as well as the development of high-power radiation sources, which are required for mm-wave and THz imaging [19, 20] and particle acceleration [21]. Periodic structures can be fabricated using copper electrodeposition methods [2, 3], chemical or laser etching [5–7] or additive manufacturing [4, 22].

This study delves into the complex field structure of the partial surface field and its potential scattering mechanisms and shows previously unpublished equations describing the complex field

structure of the surface field. We also discuss in more detail the intermediate steps between the magnetic surface current boundary condition and the definition of the complex integral term of the coupled wave equation, providing greater insight into the electromagnetic theory of the complex electrodynamic PSL structures. Experimental measurements of a planar 'air-gap' structure, which, in the absence of the dielectric substrate, is more electromagnetically similar to cylindrical PSLs than the planar PSLs mounted on substrates, are presented.

2 Theory

The 2D cylindrical PSLs that have been the subject of past and present studies and ongoing experiments at the University of Strathclyde have a cosinusoidal corrugation that can be written in the following form:

$$\tilde{r} = r_0 + \frac{\Delta r}{4}\left(e^{i\bar{m}\varphi} + e^{-i\bar{m}\varphi}\right)\left(e^{i\bar{k}_z z} + e^{-i\bar{k}_z z}\right) \quad (1)$$

where r_0 is the mean radius, Δr is the corrugation amplitude, $\bar{m}$ is the number of azimuthal periods around the circumference of the cylinder, $\bar{k}_z = 2\pi/d_z$ is the longitudinal lattice wavenumber and d_z is the lattice period. Previously, the eigenfield of a 2D PSL was described as a slowly varying wave packet $W_q(z)$ composed of oscillating terms by considering a fictitious magnetic surface current j_m. This description is valid only when the lattice corrugation Δr is suitably shallow in relation to the source wavelength, i.e. $\Delta r \ll \lambda$. The transverse electric E and magnetic H fields are expanded as a summation of the possible modes and magnetic j_m and electric j_e surface currents are considered in place of the lattice corrugation $\tilde{r}$ to simplify the geometry of the cavity to that of a smooth cylindrical waveguide. At the metal corrugation, $j_e = 0$ and hence only the j_m boundary condition applies

$$j_m = n \times (\nabla(\tilde{r}E \cdot n)) + i\omega\tilde{r}n \times [n \times H] \quad (2)$$

The normal electric field component is defined $E_n = E \cdot n$, where n is the unit vector of the normal to the unperturbed waveguide wall. In this analysis, the fictitious magnetic surface current acts as an
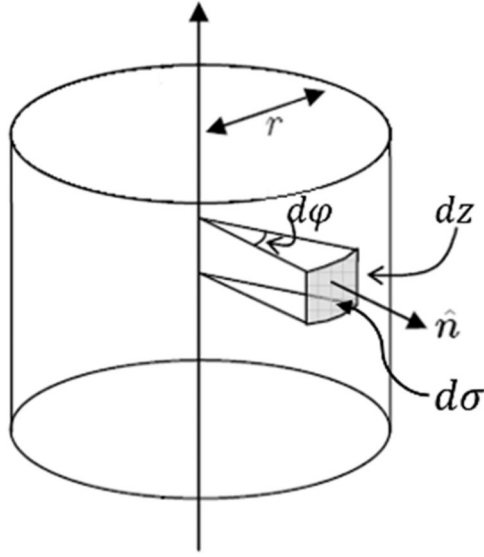
Fig. 1 *Schematic diagram showing the shaded element* $d\sigma = rd\varphi dz$ *of the integration surface*

external excitation source and a normalised wave equation is obtained by integrating the Poynting vector around the circumference of the cylinder as described in [6].

The Bragg resonance condition dictates that $\bar{k}_z = k_z^s - k_z^v$ and because we are considering a close to cut-off volume field, the resonant frequency of the surface field ω_0^s must coincide with the Bragg frequency if successful eigenmode formation is to occur. The Bragg detuning is $\bar{\delta} = \left(\omega - \sqrt{\left(\left(\omega_0^v\right)^2 + \left(\omega_0^s\right)^2\right)/2}\right)/c$. Potential sources of detuning include small ohmic, diffractive, and dissipative cavity losses. Coupling of volume and surface fields is best observed for a uniform, localised volume field with $k_z \to 0$. The uniformity of the volume field is limited by the finite length of the cavity contributing to the overall detuning. The detuning between volume and surface modes $\Delta = \left(\sqrt{\left(\left(\omega_0^s\right)^2 - \left(\omega_0^v\right)^2\right)/2}\right)/c$ has been calculated for certain planar PSL structures, where direct measurements of the partial surface field have been made. The detuning and dispersive properties of the PSL structures are considered in the analytical dispersion plots presented in Section 4.

The normalised wave equation derived in [6] is characterised by the complex integral term $\oint j_m \cdot H_q^* d\sigma$, which must be defined to obtain a complete description of the volume and surface fields that form the cavity eigenfield. Evaluation of this term necessitates taking the closed contour integral over the entire surface σ of the cylinder. By assuming that the structure is sufficiently long compared to its radius, whereby the integral contributions from the two planar, open ends of the structure can be neglected, the integral can be reduced to describe only the curved surface. We can define an element of this surface as $d\sigma = rd\varphi dz$, which is indicated by the shaded region in Fig. 1.

Considering the evaluation of the integral per unit axial length, the contour surface integral over the whole cylindrical area can, therefore, be reduced to a closed line integral over the angle $d\varphi$, where φ is the azimuthal coordinate. The closed integral over $d\varphi$ from 0 to 2π is defined in (3), where $U = j_m \cdot H_q^*$ is the integrand

$$\oint U(r, \varphi)d\sigma = \int_0^{2\pi} rU(r, \varphi)d\varphi \tag{3}$$

We obtain a general expression for the right-hand side of the wave equation given in [3, 6], where $N_{v,s} = i\omega\varepsilon/\left(\oint_{S\perp} H_q^{v,s} \cdot H_q^{*(v,s)}d\varphi\right)$ is the wave norm, which is modified to describe the volume (superscript v) or surface (superscript s) fields by multiplying by the complex conjugate of the specified field, $H_q^{*(v,s)}$

$$N_{v,s}\oint j_m \cdot H_q^* d\sigma = N_{v,s}\int_0^{2\pi} r\left(j_m \cdot H_q^*\right)\big|_{r=r_0}d\varphi \tag{4}$$

We separate j_m into two distinct terms $I_1 = n \times (\nabla(\tilde{r}E \cdot n))$ and $I_2 = i\omega\tilde{r}n \times [n \times H]$ in order to simplify this integration. Multiplying I_1 by H_q^* gives $\left[H_q^* \times (\nabla(\tilde{r}E_n))\right]n$, which can be written in the form: $\tilde{r}E_n(\nabla \times H_q^*) - \nabla \times \left((\tilde{r}E_n)H_q^*\right)$ through use of the vector identity $V \times \nabla f = f \cdot (\nabla \times V) - \nabla \times (fV)$. It is known from Maxwell's equations that $H_q^* = i\omega\varepsilon E_q^*$, which can be used to express $H_q^* I_1$ in terms of the complex conjugate of the electric field E_q^*, where $\nabla \times E_n \cdot n = 0$ to give $H_q^* I_1 = i\omega\tilde{r}E_n(E_q^* \cdot n)$. The term $H_q^* I_2$ is written in a similar manner, albeit involving the tangential magnetic field component H_τ, which results from taking the cross product of the normal unit vector n and $n \times H$ such that $n \times [n \times H] = H_\tau$ to obtain $H_q^* I_2 = i\omega\tilde{r}n \times [n \times H]H_q^* = i\omega\tilde{r}H_\tau \cdot H_{q,\tau}^*$. Together, these terms define the $j_m \cdot H_q^*$ term of the coupled wave equation, relevant to both planar and cylindrical PSLs. Expanding over the full set of modes gives

$$j_m \cdot H_q^* = i\omega\tilde{r}(z, \varphi)\left(\sum_q W_q(z)E_{q,n} \cdot E_{q,n}^* + \sum_q W_q(z)H_{q,\tau} \cdot H_{q,\tau}^*\right) \tag{5}$$

where $E_{q,n}^*$ and $H_{q,\tau}^*$ are the complex conjugates of the normal electric field and tangential magnetic field components for the close to cut-off (qth) mode, respectively. When considering an azimuthally symmetric and close to cut-off volume field, where $k_z \cong 0$ and $E_{q,n} = 0$, we can write

$$j_m \cdot H_q^* = i\omega\tilde{r}(z, \varphi)\sum_q W_q(z)H_{q,\tau} \cdot H_{q,\tau}^* \tag{6}$$

The tangential magnetic field component can be separated into its tangential magnetic volume and surface field components. The cosinusoidal corrugation $\tilde{r}$ inscribed on the inner cavity wall and defined in (1) is substituted into (6) to give

$$j_m \cdot H_q^* = i\omega\left[r_0 + \frac{\Delta r}{4}\left(e^{i\bar{m}\varphi} + e^{-i\bar{m}\varphi}\right)\left(e^{i\bar{k}_z z} + e^{-i\bar{k}_z z}\right)\right]$$

$$H_{q,\tau}^{*,v;s} \cdot \left(H_{q,\tau}^v(r)\sum_{n_v} A_{n_v}(z)e^{in_v\bar{k}_z z}\right.$$

$$\left. + H_{q,\tau}^s(r)\cos m_s\varphi \sum_{n_s} B_{n_s}(z)e^{in_s\bar{k}_z z}\right) \tag{7}$$

where $\sum_{n_v} A_{n_v}(z)e^{in_v\bar{k}_z z}$ and $\sum_{n_s} B_{n_s}(z)e^{in_s\bar{k}_z z}$ are Fourier expansions describing the spatial harmonics of the slowly evolving volume and surface fields along the longitudinal direction and $A(z)$ and $B(z)$ denote the volume and surface field amplitudes, respectively. The complex conjugate of the tangential magnetic field $H_{q,\tau}^{*,v;s}$ is written $H_{q,\tau}^{*,v}$ or $H_{q,\tau}^{*,s}$ depending on whether the volume field is scattering into the surface field or vice versa.

At this stage, we average over the fast oscillation terms from 0 to 2π to eradicate the exponential terms that would otherwise integrate to zero. In [6], we described the scattering associated with the fundamental harmonic of the volume field and then considered the more general cases of volume and surface field scattering. Here, we take a more detailed approach, this time describing the fundamental harmonic of the surface field $n_s = 0$ interacting with the $n_v = \pm 1$ spatial harmonics of the volume field and presenting previously unpublished equations that give further insight into the complex field coupling. To describe the forward and backward scattering of the surface field with wave norm $\tilde{N}_s = -\omega^2\varepsilon/\left(\oint_{S\perp} H_q^s \cdot H_q^{*,s}d\varphi\right)$ we express $\oint j_m \cdot H_q^* d\sigma$ as

$$\oint \boldsymbol{j_m} \cdot \boldsymbol{H_q^*} \mathrm{d}\sigma = \tilde{N}_S \int_0^{2\pi} r \Big[r_0 + \frac{\Delta r}{4} \big(\mathrm{e}^{\mathrm{i}\bar{m}\varphi} + \mathrm{e}^{-\mathrm{i}\bar{m}\varphi} \big) \big(\mathrm{e}^{\mathrm{i}\bar{k}_z z} + \mathrm{e}^{-\mathrm{i}\bar{k}_z z} \big) \Big]$$

$$\boldsymbol{H_{q,\tau}^{*,s}}(r,\varphi) \cdot \Bigg(\boldsymbol{H_{q,\tau}^{v}}(r) \sum_{n_v} A_{n_v}(z) \mathrm{e}^{\mathrm{i}n_v \bar{k}_z z} \tag{8}$$

$$+ \boldsymbol{H_{q,\tau}^{s}}(r) \cos m_s \varphi \sum_{n_s} B_{n_s}(z) \mathrm{e}^{\mathrm{i}n_s \bar{k}_z z} \Bigg) \Bigg| r = r_0 \mathrm{d}\varphi$$

which, when taking into account that $\boldsymbol{H_{q,\tau}^{*,s}}(r,\varphi) = \boldsymbol{H_{q,\tau}^{*,s}}(r)\cos\bar{m}\varphi$ and expanding the brackets can be written in the form $\oint \boldsymbol{j_m} \cdot \boldsymbol{H_q^*} d\sigma = \tilde{N}_s r_0^2 \int_0^{2\pi} X|_{r=r_0} \mathrm{d}\varphi$, where X is the integrand, comprising terms (i)–(iv).

(i) $\boldsymbol{H_{q,\tau}^{*,s}}(r_0)\cos\bar{m}\varphi\, \boldsymbol{H_{q,\tau}^{v}}(r_0)\sum_2 W_q^v(z)$

(ii) $\boldsymbol{H_{q,\tau}^{*,s}}(r_0)\cos\bar{m}\varphi\, \boldsymbol{H_{q,\tau}^{s}}(r_0)\cos\bar{m}\varphi \sum_{n_s} B_{n_s}(z)\mathrm{e}^{\mathrm{i}n_s\bar{k}_z z}$

(iii) $\dfrac{\Delta r}{4r_0}\big(\mathrm{e}^{\mathrm{i}\bar{m}\varphi} + \mathrm{e}^{-\mathrm{i}\bar{m}\varphi}\big)\big(\mathrm{e}^{\mathrm{i}\bar{k}_z z} + \mathrm{e}^{-\mathrm{i}\bar{k}_z z}\big)\boldsymbol{H_{q,\tau}^{*,s}}(r_0)\cos\bar{m}\varphi$

$\quad\quad \boldsymbol{H_{q,\tau}^{v}}(r_0)\sum_{n_v} A_{n_v}(z)\mathrm{e}^{\mathrm{i}n_v\bar{k}_z z}$

(iv) $\dfrac{\Delta r}{4r_0}\big(\mathrm{e}^{\mathrm{i}\bar{m}\varphi} + \mathrm{e}^{-\mathrm{i}\bar{m}\varphi}\big)\big(\mathrm{e}^{\mathrm{i}\bar{k}_z z} + \mathrm{e}^{-\mathrm{i}\bar{k}_z z}\big)\boldsymbol{H_{q,\tau}^{*,s}}(r_0)\cos\bar{m}\varphi$

$\quad\quad \boldsymbol{H_{q,\tau}^{s}}(r_0)\cos m_s\varphi \sum_{n_s} B_{n_s}(z)\mathrm{e}^{\mathrm{i}n_s\bar{k}_z z}$

Term (i) is at once neglected on the basis that $\int_0^{2\pi}(\cos\bar{m}\varphi)\,\mathrm{d}\varphi = 0$ following integration. The integrand is further simplified by eliminating (iv), which contains only surface field terms, since the inclusion of $(\Delta r/4r_0)$, which partly determines the strength of the coupling between the partial volume and surface fields, requires both volume and surface field components. Mathematically, $\mathrm{e}^{\mathrm{i}n_s\bar{k}_z z}\big(\mathrm{e}^{\mathrm{i}\bar{k}_z z} + \mathrm{e}^{-\mathrm{i}\bar{k}_z z}\big) \neq 0$ when $n_s = 0$ and (iv) vanishes after integration. In (ii) the Fourier expansion describing the slowly changing surface field is reduced to B_0 when considering the fundamental surface field harmonic and we rewrite the expression in cosine notation using the trigonometric identity $2\cos\bar{m}\varphi = \big(\mathrm{e}^{\mathrm{i}\bar{m}\varphi} + \mathrm{e}^{-\mathrm{i}\bar{m}\varphi}\big)$ to obtain (see (9)) . Prior studies have shown that the fundamental surface field harmonic interacts with the ± 1 spatial harmonics of the volume field and vice versa [3, 6]. The fast oscillation terms along the z-coordinate are expanded for the $n_v = \pm 1$ volume field harmonics to get $\mathrm{e}^{\mathrm{i}n_v\bar{k}_z z}\big(\mathrm{e}^{\mathrm{i}\bar{k}_z z} + \mathrm{e}^{-\mathrm{i}\bar{k}_z z}\big) = 1 + \mathrm{e}^{\pm 2\mathrm{i}\bar{k}_z z}$. The remaining exponential term then disappears after integration. The definition of $\boldsymbol{j_m} \cdot \boldsymbol{H_q^*}$ for the particular case of the fundamental surface field harmonic scattering into the $n_v = \pm 1$ volume field harmonics is given by

$$\boldsymbol{j_m} \cdot \boldsymbol{H_q^*} = \pi\tilde{N}_s r_0^2 \Bigg(\boldsymbol{H_{q,\tau}^{*,s}}(r_0) \cdot \boldsymbol{H_{q,\tau}^{s}}(r_0) B_0(z)$$
$$+ \frac{\Delta r}{2r_0} \boldsymbol{H_{q,\tau}^{*,s}}(r_0) \cdot \boldsymbol{H_{q,\tau}^{v}}(r_0) \sum_{n_v} A_{n_v}(z) \Bigg) \tag{10}$$

The first part of the equation describes the surface field formed from the tangential component around the azimuth and the slowly varying surface field amplitude in the longitudinal direction. This

provides a full description of the localised surface field accumulating at the corrugation that does not involve the volume field or contribute to the coupling. The second term describes the resonant scattering of the surface field into the volume field that leads to the excitation of a coupled, single cavity eigenmode. More generally, the scattering of the surface field into the volume field is investigated by multiplying the surface field components by $\mathrm{e}^{-\mathrm{i}n_s\bar{k}_z z}$ and discarding the terms that integrate to 0. Taking into account that $\mathrm{e}^{-\mathrm{i}n_s\bar{k}_z z} \cdot \mathrm{e}^{\mathrm{i}n_s\bar{k}_z z} = 1$, we obtain

$$\oint \boldsymbol{j_m} \cdot \boldsymbol{H_q^*} \mathrm{d}\sigma = r_0^2 \tilde{N}_S \int_0^{2\pi} \Bigg(\frac{\Delta r}{2r_0}\cos\bar{m}\varphi\big(\mathrm{e}^{\mathrm{i}\bar{k}_z z(1-n_s+n_v)} + \mathrm{e}^{-\mathrm{i}\bar{k}_z z(1+n_s-n_v)}\big)$$

$$\boldsymbol{H_{q,\tau}^{*,s}}(r_0)\cos\bar{m}\varphi\, \boldsymbol{H_{q,\tau}^{v}}(r_0) \sum_{n_v=-\infty}^{\infty} A_{n_v}(z)$$

$$\boldsymbol{H_{q,\tau}^{*,s}}(r_0)\cos\bar{m}\varphi\, \boldsymbol{H_{q,\tau}^{s}}(r_0)\cos\bar{m}\varphi \sum_{n_s} B_{n_s}(z) \Bigg) \mathrm{d}\varphi$$

$$\tag{11}$$

which, after integration, leads to the derivation of a coupled wave equation describing the scattering of either the fundamental surface field or the ± 2 spatial harmonics of the surface field into the ± 1 spatial harmonics of the volume field [6].

3 Experimental measurement of PSL structure

The theory describing the coupled eigenfield of a 2D PSL is relevant to structures of both planar and cylindrical geometry in the case of the large radius approximation. It is known that planar PSLs can be converted to cylindrical PSLs using the conformal mapping method. The structures with the two different geometries are both over-moded but in the case of the planar structure, the volume field is less well defined and a dielectric substrate has previously [5–7] been used to support field confinement via internal reflection. The planar PSLs were designed under the assumption that the periodicity d_z of the lattice governs the wavelength of the localised surface field λ_s inside each lattice cell such that $\lambda_s \simeq d_z$. The PSLs can be likened to an array of rectangular waveguide apertures where the reflected frequency is close to the cut-off of the fundamental waveguide mode [5].

Here, we compare the results for the planar PSL with period 1.94 mm, mounted on the copper-backed, 0.76 mm thick FR-4 substrate to a tunable 'air-gap' PSL structure composed of a 2D PSL with period 1.94 mm, held by four nylon screws at a variable distance from a copper backplate, as illustrated in Fig. 2. The air separation was adjusted to ~1.6 mm to maintain an equivalent optical path length to that of the 0.76 mm FR-4 substrate used in similar PSL structures [5, 6]. For the 'air-gap' structure, the PSL was etched onto a thicker, 0.3 mm copper layer (compared to the 35 μm thick copper used in the PSLs with copper backed substrates) in order to provide sufficient amplitude and therefore coupling of the surface field in the absence of the dielectric. A full description of the manufacturing and experimental techniques relating to the fabrication and measurement of the planar PSLs is given in [5].

Fig. 3 shows measurements made using a vector network analyser (VNA) and a pair of high-frequency modules assembled with two 140-220 GHz standard 20 dBi gain rectangular horn antennae transmitting and receiving, respectively, a plane-polarised wave with the electric field vector orthogonal to the plane of incidence. For these reflection measurements, the transmitting and receiving antennae were carefully positioned with an equal angle of incidence and reflection and both at the same distance from the

$$\oint \boldsymbol{j_m} \cdot \boldsymbol{H_q^*} \mathrm{d}\sigma = \tilde{N}_S r_0^2 \Bigg(\boldsymbol{H_{q,\tau}^{*,s}}(r_0) \cdot \boldsymbol{H_{q,\tau}^{s}}(r_0) B_0(z) \int_0^{2\pi} \Big(\frac{1}{2} + \frac{1}{2}\cos\bar{m}\varphi \Big) \mathrm{d}\varphi \Bigg)$$

$$+ \int_0^{2\pi} \Bigg(\frac{\Delta r}{2r_0} \big(\mathrm{e}^{\mathrm{i}\bar{k}_z z} + \mathrm{e}^{-\mathrm{i}\bar{k}_z z} \big) \boldsymbol{H_{q,\tau}^{*,s}}(r_0) \boldsymbol{H_{q,\tau}^{v}}(r_0) \cos^2\bar{m}\varphi \sum_{n_v} A_{n_v}(z) \mathrm{e}^{\mathrm{i}n_v\bar{k}_z z} \Bigg) \mathrm{d}\varphi \tag{9}$$
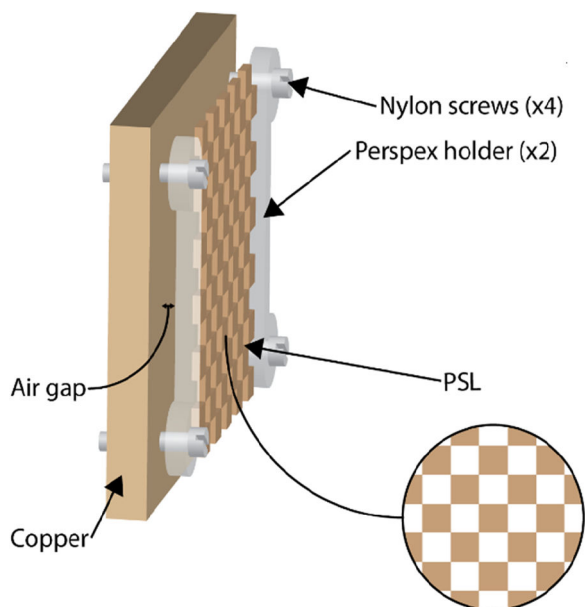
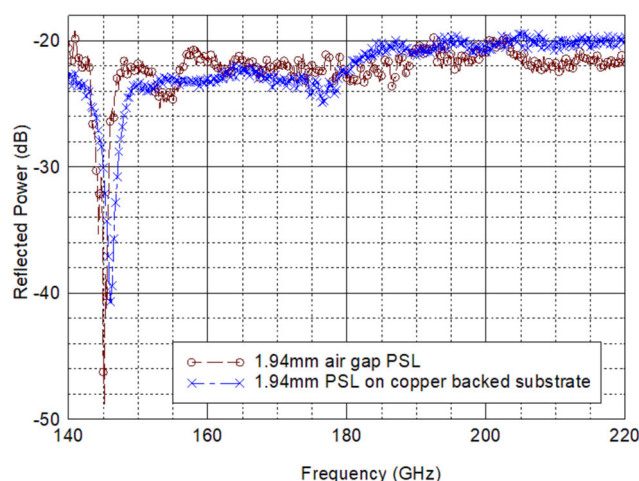**Fig. 2** *Schematic diagram showing 'air-gap' PSL structure with period 1.94 mm*

Fig. 3 *Reflection measurements for the 1.94 mm 'air-gap' PSL (red trace) and the 1.94 mm PSL (blue trace) mounted on a copper backed dielectric substrate*
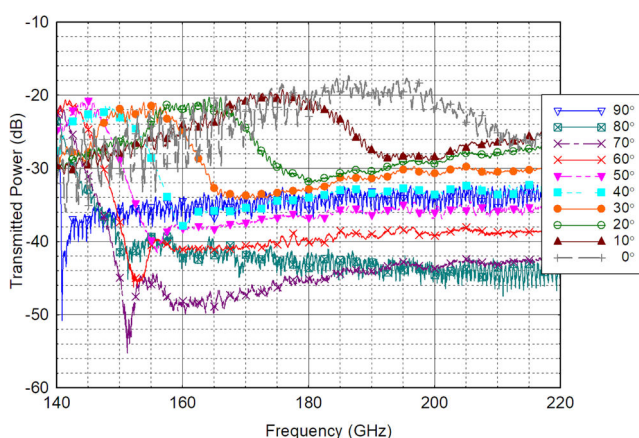

Fig. 4 *Transmission measurements for the 1.94 mm mesh PSL (no metal back plate) showing surface field at different irradiation angles (0°–90°)*

PSL, just within the farfield [5, 7]. Transmission measurements (Fig. 4) were made only for the mesh PSL with no metal backplate

and in this arrangement, the transmitting and receiving antennae were directly aligned with the PSL equidistant between the two antennae and rotated through an angular range of 0°–90°. The VNA was calibrated to operate within the 140–220 GHz frequency range and measurements were made for both the 'air-gap' PSL (red trace) and the conventional PSL (blue trace) at a fixed incident and measurement angle of 60°.

A high-Q resonance is observed at 145 GHz for the 'air-gap' PSL and 146 GHz for the conventional 1.94 mm PSL etched on the dielectric substrate. This frequency is different from that of the surface field at 60° (141 GHz), which has been measured directly in a 1.94 mm mesh PSL (equivalent to the 'air-gap' PSL without the copper backplate) as shown in Fig. 4. The results for the two PSL structures are in close agreement with a frequency discrepancy of just 1 GHz, which may arise due to the minor changes in experimental alignment, suggesting that the 'air-gap' structure has the potential to support volume and surface field coupling at some angles.

We note that the reflected power for the 'air-gap' structure (∼ −49 dB) is substantially greater than that for the PSL with the dielectric substrate (∼−41 dB), which may occur due to a reduction in dielectric losses. However, despite smaller dielectric losses, the 'air-gap' structure does not support eigenmode formation and 'mode-locking' at all angles unlike the metal-substrate backed PSLs [5–7], possibly due to more energy escaping from the unbound edges at certain angles. Also, without the dielectric providing the spacing between the two planar surfaces, it is more difficult to maintain the uniform separation required to control the frequency definition of the volume mode over the area of the planar structure.

Nevertheless, since these 'air-gap' planar PSLs closely approximate electromagnetically to 'vacuum-gap' planar PSLs, the results show potential for 'vacuum-gap' planar PSLs to be combined with a sheet electron beam [23] and, therefore, incorporated into high-power radiation sources. The applications in high-power radiation sources are in addition to the wide-ranging applications that include solar cells, filters, and perfect absorbers.

In our previous work, only cylindrical 'meta-dielectric' PSLs constructed solely from conducting material, e.g. copper, with no dielectric lining were considered for high-power radiation sources. Owing to the 'oversized' radius r of the cylindrical structures ($r \gg \lambda$), a 'quasi-planar' approximation can be applied [2, 3, 6, 8, 9], where the cylindrical structure is described by a planar PSL, without a dielectric substrate. The 'air-gap' planar PSL, therefore, more closely resembles the 2D cylindrical PSLs used in electron beam driven experiments at the University of Strathclyde [4], than the previous planar PSLs with dielectric substrates, since here no dielectric material is included and the corrugated surface structure behaves as a 'meta-dielectric'.

The ability to adjust conveniently the separation between the PSL and the metal backing means that a structure of this type could possibly be used to compensate for the detuning associated with the difference in angular frequency of the volume and surface fields by subtly adjusting the separation between the PSL and the metal backplate to observe optimum coupling. This could be advantageous in applications where a specific eigenmode frequency is required.

4 Analytical dispersion plots

In the coupled eigenfield dispersion equation presented in [3, 6], the detuning parameters have been renormalised using division by the parameter $\bar{K}$, where $\bar{K} = \Omega/c$ and

$$\Omega = \sqrt{\frac{\left(\omega_0^v\right)^2 + \left(\omega_0^s\right)^2}{2}} \tag{12}$$

The renormalised Bragg detuning parameter δ and the detuning of the volume and surface field angular cut-off frequencies $\widetilde{\Delta}$ are written

$$\delta = \left(\omega - \left(\frac{(\omega_0^v)^2 + (\omega_0^s)^2}{2}\right)^{1/2}\right) \Big/ \left(\frac{(\omega_0^v)^2 + (\omega_0^s)^2}{2}\right)^{1/2} \tag{13a}$$

$$= \frac{\omega - \Omega}{\Omega}$$

$$\widetilde{\Delta} = \left(\frac{(\omega_0^s)^2 - (\omega_0^v)^2}{2}\right)^{1/2} \Big/ \left(\frac{(\omega_0^v)^2 + (\omega_0^s)^2}{2}\right)^{1/2} \tag{13b}$$

The overall detuning $\Gamma = 2\bar{k}_z c / \left((\omega_0^v)^2 + (\omega_0^s)^2\right)^{1/2}$ takes into account the permittivity, substrate thickness (or air separation), and lattice periodicity. The present analytical study has been carried out assuming that $\alpha \sim 0.45$ [6]. A unit cell of the planar PSL was modelled with periodic boundaries using the electromagnetic solver CST Microwave Studio and eigenmode calculations over a large number of modes were used to establish the approximate cut-off frequency of the volume field at an incident angle of 0°. The surface field, observed exclusively in the 1.94 mm mesh PSL, exists within the region of 185–200 GHz at 0°. The analytical dispersions at 0° differ from the experimental measurements shown in Fig. 3, which were made at oblique incident angles. The volume field eigenmode calculations performed using CST MWS are also applicable to the case of an incident angle of 0°, but serve as a good approximation for the cut-off frequency of the partial volume field at all incident angles.

The transmission measurements [24] of Fig. 4 showed that the frequency of the surface field at normal incidence is much higher than predicted by the $\lambda_s \simeq d_z$ approximation [5], which in turn affects the detuning and dispersive properties. Provided with an initial value of the renormalised Bragg detuning δ, the dispersion equation [3, 6] is solved over a number of data points by increasing δ in small increments $\delta = \delta + \Delta\delta$ and solving for the normalised wave vector Λ for each value of δ. For every iteration, k_z and ω are evaluated from the relations

$$k_z = \frac{\Lambda}{c}\left(\frac{(\omega_0^v)^2 + (\omega_0^s)^2}{2}\right)^{1/2} \tag{14a}$$

$$\omega = \delta\left(\frac{(\omega_0^v)^2 + (\omega_0^s)^2}{2}\right)^{1/2} + \left(\frac{(\omega_0^v)^2 + (\omega_0^s)^2}{2}\right)^{1/2} \tag{14b}$$

Analytical dispersion diagrams for the 'air-gap' structure at 0° and 60°, both for separation of 1.6 mm, are presented in Figs. 5a and b, respectively. The solid black traces represent the coupled eigenfield dispersion, while the dashed and dot-dashed grey traces show the uncoupled surface and volume field dispersions, respectively. The surface field is characterised by an imaginary transverse wavenumber and the surface field spatial harmonics are evident at large values of k_z.

Fig. 5a shows the dispersion diagram for the 'air-gap' structure at 0° when $\Gamma < \sqrt{2}$ and $\widetilde{\Delta} = 0.53$. The surface field harmonics cross one another below the cut-off frequency of the uncoupled volume field, distorting the overall appearance of the dispersion. We note that $\Gamma \sim \sqrt{2}$ when the periodicity of the PSL is chosen such that $(\bar{k}_z)^2 = (k_\perp^v)^2 + (k_\perp^s)^2$, where $k_\perp^v$ and $k_\perp^s$ are the transverse wavenumbers of the volume and surface fields. The number of coupled dispersion branches and their frequency location are influenced by where the surface field harmonics intersect one another. The surface field frequency and parameter values of both Γ and $\widetilde{\Delta}$ predict the frequencies and wavenumbers at which coupled eigenfield solutions exist. Different dispersive properties are typically observed as Γ is increased beyond $\sqrt{2}$ and the surface field harmonics intersect at higher frequencies.

The dispersion for the 'air-gap' structure at 60° where $\Gamma \sim \sqrt{2}$ and $\widetilde{\Delta} = 0.36$ is provided in Fig. 5b. Owing to the reduced frequency separation between the volume and surface fields at the larger incident angle, the surface field harmonics intersect at a higher frequency. Here, a backward wave interaction with an
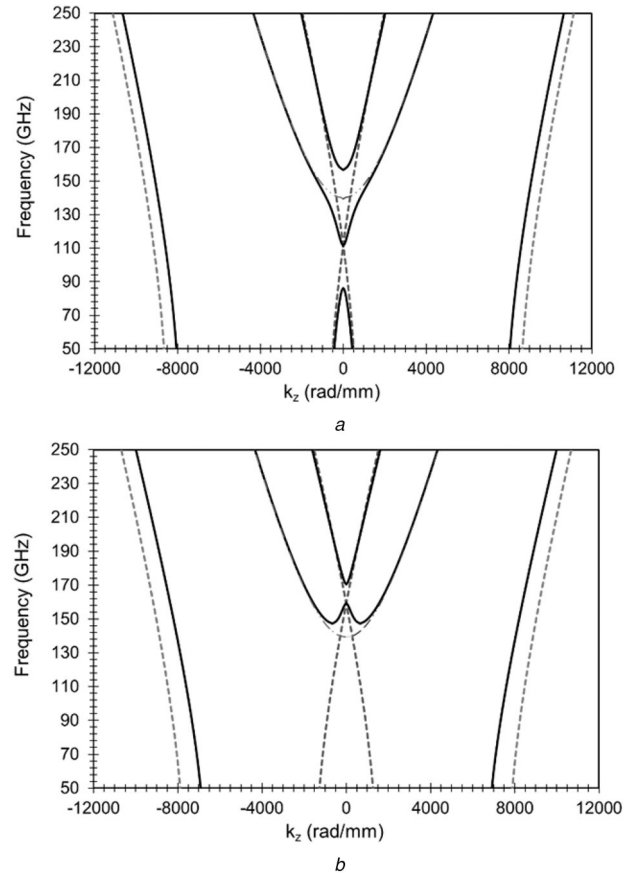

Fig. 5 *Analytical dispersion for 1.94 mm 'air-gap' PSL at*
(a) 0°, (b) 60°

electron beam is viable, demonstrating that, if the planar air-gap PSL is intended for use in a novel radiation source in combination with a sheet electron beam, the PSL must be positioned at a suitable angle from the excitation source.

5 Conclusion

Complex integral equations describing the surface field scattering into the volume field are presented in this study. The surface field is studied experimentally through the use of a novel 2D 'air-gap' PSL structure, which more closely resembles the 2D cylindrical PSL structures used in the electron beam driven experiments and without the dielectric material, the corrugated surface behaves more like a meta-dielectric. Transmission measurements show the surface field frequency shifting significantly, depending on the irradiation angle. Despite the absence of a dielectric substrate, it has been shown that the coupling of the surface field with a weakly defined volume field formed between the two planar copper layers is still possible, resulting in a coupled cavity eigenmode at an irradiation angle of 60°.

It has been shown both experimentally and analytically by solving the coupled dispersion equation that volume and surface field coupling in the 'air-gap' structure is most effective at more oblique incident angles where there is less frequency disparity between the volume and surface fields. The coupled dispersion analysis demonstrates that a backward slow-wave interaction with an electron beam is feasible. The planar 'air-gap' PSL discussed in this study is relevant to a number of electromagnetic applications including novel, high-power mm-wave and THz radiation sources, solar cells, 'perfect' absorbers, and tunable filters.

6 Acknowledgments

7 References

[1] Ginzburg, N.S., Peskov, N.Y., Sergeev, A.S., *et al.*: 'The use of a hybrid resonator consisting of one-dimensional and two-dimensional Bragg reflectors for generation of spatially coherent radiation in a coaxial free-electron laser', *Phys. Plasmas*, 2002, **9**, (6), pp. 2798–2802

[2] Konoplev, I.V., MacLachlan, A.J., Robertson, C.W., *et al.*: 'Cylindrical periodic surface lattice as a metadielectric: concept of a surface-field cherenkov source of coherent radiation', *Phys. Rev. A*, 2011, **84**, (1), p. 013826

[3] Konoplev, I.V., MacLachlan, A.J., Robertson, C.W., *et al.*: 'Cylindrical, periodic surface lattice—theory, dispersion analysis, and experiment', *Appl. Phys. Lett.*, 2012, **101**, p. 121111

[4] Phipps, A.R., MacLachlan, A.J., Robertson, C.W., *et al.*: 'Electron beam excitation of coherent sub-terahertz radiation in periodic structures manufactured by 3D printing', *Nucl. Instrum. Methods Phys. Res. B*, 2017, **402**, pp. 202–205

[5] MacLachlan, A.J., Robertson, C.W., Cross, A.W., *et al.*: 'Volume and surface mode coupling experiments in periodic surface structures for use in mm-THz high power radiation sources', *AIP Adv.*, 2018, **8**, (10), p. 105115

[6] MacLachlan, A.J., Robertson, C.W., Konoplev, I.V., *et al.*: 'Resonant excitation of volume and surface fields on complex electrodynamic surfaces', *Phys. Rev. Appl.*, 2019, **11**, (3), p. 034034

[7] MacLachlan, A.J., Robertson, C.W., Ronald, K., *et al.*: 'Mode coupling in periodic surface lattice and metamaterial structures for mm-wave and THz applications', *SN Appl. Sci.*, 2019, **1**, (6), p. 613

[8] Ginzburg, N.S, Malkin, A.M., Sergeev, A.S., *et al.*: 'Oversized coaxial and cylindrical surface-wave oscillators with two-dimensional periodical grating (quasioptical model)', *J. Appl. Phys.*, 2013, **113**, p. 104504

[9] Ginzburg, N.S, Ilyakov, E.V., Kulagin, I.S., *et al.*: 'Theoretical and experimental studies of relativistic oversized Ka-band surface-wave oscillator based on 2D periodical corrugated structure', *Phys. Rev. Spec. Top., Accel. Beams*, 2018, **21**, p. 080701

[10] Liu, S., Zhang, P., Liu, W., *et al.*: 'Surface polariton Cherenkov light radiation source', *Phys. Rev. Lett.*, 2012, **109**, p. 153902

[11] Van Lare, M., Lenzmann, F., Verschuuren, M.A., *et al.*: 'Mode coupling by plasmonic surface scatterers in thin-film silicon solar cells', *Appl. Phys. Lett.*, 2012, **101**, p. 221110

[12] Landy, N.I., Sajuyigbe, S., Mock, J.J., *et al.*: 'Perfect metamaterial absorber', *Phys. Rev. Lett.*, 2008, **100**, p. 207402

[13] Kong, H., Jin, Z., Li, G., *et al.*: 'Polarization-independent metamaterial absorber for terahertz frequency', *J. Infrared Millim. Terahertz Waves*, 2012, **33**, (6), pp. 649–656

[14] Shoaib, S., Shoaib, N., Shoaib, I., *et al.*: 'Design and performance analysis of pattern reconfigurable MIMO antennas for mobile smartphones', *Microw. Opt. Technol. Lett.*, 2017, **59**, (1), pp. 148–156

[15] Ulrich, R.: 'Interference filters for the far infrared', *Appl. Opt.*, 1968, **7**, (10), pp. 1987–1996

[16] Ulrich, R.: 'Far-infrared properties of metallic mesh and its complementary structure', *Infrared Phys.*, 1967, **7**, (1), pp. 37–55

[17] Ri-Hui, X., Jiu-Sheng, L., 'Double-layer frequency selective surface for terahertz bandpass filter', *J. Infrared Millim. Terahertz Waves*, 2018, **39**, (10), pp. 1039–1046

[18] Carelli, P., Chiarello, F., Cibella, S., *et al.*: 'A fast terahertz spectrometer based on frequency selective surface filters', *J. Infrared Millim. Terahertz Waves*, 2012, **33**, (5), pp. 505–512

[19] Abraham, E., Younus, A., Fatimy, A. El., *et al.*: 'Broadband terahertz imaging of documents written with lead pencils', *Opt. Commun.*, 2009, **282**, p. 3104

[20] Seco-Martorell, C., Lopez-Domınguez, V., Arauz-Garofalo, G., *et al.*: 'Goya's artwork imaging with terahertz waves', *Opt. Exp.*, 2013, **21**, (15), pp. 17800–17805

[21] York, A.G., Milchberg, H.M., Palastro, J.P., *et al.*: 'Direct acceleration of electrons in a corrugated plasma waveguide', *Phys. Rev. Lett.*, 2008, **100**, (19), p. 195001

[22] French, D.M., Shiffler, D.: 'High power microwave source with a three dimensional printed metamaterial slow-wave structure', *Rev. Sci. Instrum.*, 2016, **87**, p. 053308

[23] Peskov, N.Yu., Arzhannikov, A.V., Ginzburg, N.S., *et al.*: 'Development of powerful W-band planar surface-wave oscillator driven by high-current relativistic sheet electron beam'. 44th Int. Conf. Infrared, MM and THz Waves, Paris, France, September 2019

[24] MacLachlan, A.J., Robertson, C.W., Cross, A.W., *et al.*: Data underpinning this publication is available from the University of Strathclyde KnowledgeBase. Available at https://doi.org/10.15129/e7ffa36b-c515-4e2c-bc77-c120451f41ed

1156

IET Microw. Antennas Propag., 2020, Vol. 14 Iss. 11, pp. 1151-1156